Insect-scale jumping robots enabled by a dynamic buckling cascade

Yuzhe Wang[a,1] (ID), Qiong Wang[a,1] (ID), Mingchao Liu[b] (ID), Yimeng Qin[a], Liuyang Cheng[a], Ophelia Bolmin[a] (ID), Marianne Alleyne[c] (ID), Aimy Wissa[d], Ray H. Baughman[e] (ID), Dominic Vella[b] (ID), and Sameh Tawfick[a,2] (ID)

Millions of years of evolution have allowed animals to develop unusual locomotion capabilities. A striking example is the legless-jumping of click beetles and trap-jaw ants, which jump more than 10 times their body length. Their delicate musculoskeletal system amplifies their muscles' power. It is challenging to engineer insect-scale jumpers that use onboard actuators for both elastic energy storage and power amplification. Typical jumpers require a combination of at least two actuator mechanisms for elastic energy storage and jump triggering, leading to complex designs having many parts. Here, we report the new concept of dynamic buckling cascading, in which a single unidirectional actuation stroke drives an elastic beam through a sequence of energy-storing buckling modes automatically followed by spontaneous impulsive snapping at a critical triggering threshold. Integrating this cascade in a robot enables jumping with unidirectional muscles and power amplification (JUMPA). These JUMPA systems use a single lightweight mechanism for energy storage and release with a mass of 1.6 g and 2 cm length and jump up to 0.9 m, 40 times their body length. They jump repeatedly by reengaging the latch and using coiled artificial muscles to restore elastic energy. The robots reach their performance limits guided by theoretical analysis of snap-through and momentum exchange during ground collision. These jumpers reach the energy densities typical of the best macroscale jumping robots, while also matching the rapid escape times of jumping insects, thus demonstrating the path toward future applications including proximity sensing, inspection, and search and rescue.

jumping robot | jumping insect | insect-scale robot | artificial muscles | snap-through

Jumping locomotion is common in animals, including insects, despite their vastly different kinematic and biological mechanisms (1–7). In squat jumping, most large animals rely on quickly generating a large momentum by pushing most of their mass with a high vertical velocity, constrained by the stroke (motion range) and power of their muscles. Due to this high rate of motion, high stresses are generated in the animals' intricate body parts. Jumping hence presents an extremely challenging mechanical task and requires stringent material constraints. Despite their small size, insects are phenomenal jumpers in comparison to large squat jumpers: They routinely reach heights exceeding 10 times their body length, and reaching in some cases 30 times their length, which is equivalent to a human jumping up to the 15th floor of a building. Through evolution, these jumping skills enabled insects to survive in diverse environments. As a primary form of locomotion, jumping helps them escape from predators, right themselves, catch prey, or adapt to unfamiliar terrain. Recent studies have revealed the jumping mechanisms of various insects (8–12). Many insects, such as locusts and fleas, initiate jumping by the traditional means of jointed appendages (9, 11). In contrast, click beetles (a term describing approximately 10,000 species worldwide) (*Coleoptera: Elateridae*) can jump without using any appendages; instead, they quickly snap their bodies, producing an audible click as well as a jump. The jump of click beetles is enabled by skeletal muscle, which slowly stores elastic energy in their body and thoracic hinge leaving the body in a bent position (the "latched" position, Fig. 1 *A, ii*). When triggered, the latch is released, and the body of the beetle unbends extremely quickly (Fig. 1 *A, iii*), accelerating the center of mass of the click beetle upward and resulting in a powerful jump (Fig. 1 *A, iv*) for hunting, escape, or other activities (2, 8, 13, 14). Fig. 1*A* and *SI Appendix*, Fig. S1 show snapshots of the takeoff sequence of an *Alaus oculatus* (mass = 754 mg, and body length = 31 mm) click beetle. The snapshots show the extremely fast unbending movement which results in the center of mass acceleration and legless jump. Beetles amplify the power of muscle, storing energy slowly before releasing it rapidly. In this paper, we present a robot inspired by the click beetles' energy storage and take-off process, including its ability to perform legless jumping by using muscles to store elastic energy that is released in a jump.

Significance

Fleets of insect-scale robots could perform unique functions enabled by their size to address needs in agriculture, inspection in restricted spaces, and search and rescue. Inspired by recent advances in understanding the mechanism of power amplification in jumping beetles and ants, we conceive and realize a jumping robot that matches or surpasses both natural creatures and robots. The jumping mechanism uses dynamic buckling cascading and allows for a single stroke from a coiled artificial muscle to actuate an automatic sequence of shape transformations in a buckling beam. This mechanism stores large elastic energy in miniature robots, which match the energy density of macroscale robots, while maintaining the small size, extreme acceleration, and fast escape response times of insects.
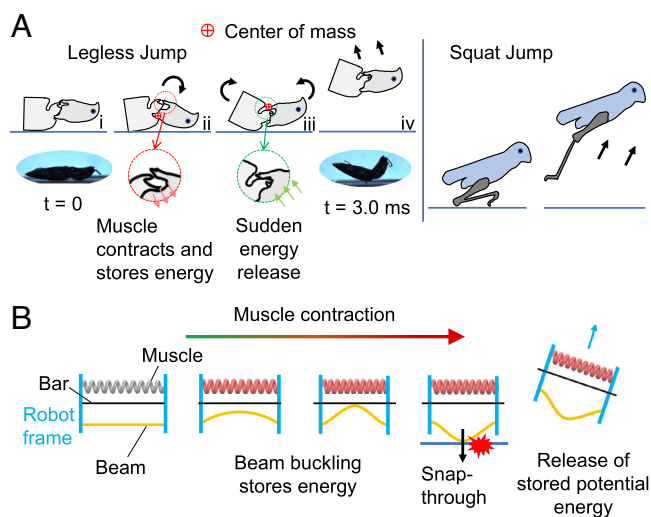
Biologically inspired millimeter-scale jumpers (15–18) aim to mimic insects' unique ability to navigate highly textured environments (19, 20). Owing to their small size (and hence diminished inertial forces at the millimeter scale), they are expected to be potentially more resilient in landing or colliding with obstacles (21). A notable recent study considered the limits of biological jumping, and even engineered a small device that jumps 30 m using a ratchet (22). Although several jumping mechanisms inspired by animal species have been demonstrated (18, 23), small-scale jumping robots with integrated actuation, energy storage, and release mechanism have limited performance. Moreover, mimicking the jumping of legless organisms such as click beetles remains challenging at both large and small scales (24). These limitations on integrated small-scale jumpers are caused by the need to combine at least two separate mechanisms into a successful jumper: i) an actuator mechanism for storing large potential energy while preventing premature release, ii) an actuator mechanism for triggering the rapid release of potential energy as kinetic energy. Each mechanism includes an actuator and a mechanical linkage, in addition to an energy storage element like a spring. This complicates the design, adds mass, and requires many small delicate parts beyond the limit of current fabrication and materials that can handle (i) and (ii) without damage.

To enable jumpers with fully integrated actuators and mechanisms, we introduce an unusual "dynamic buckling cascade" mechanism which enables high elastic energy storage (in the static cascade) as well as faster release and higher jumping than previous small-scale robots via the dynamic snap-through at the end of the cascade. Dynamic buckling cascading entails a beam which buckles to one side then pushes against a confining rigid rail; this drives the robot through an automatically triggered sequence of distinct static buckling modes, called a cascade, ultimately leading to an impulsive release of the stored energy at a critical threshold as the beam "snaps" to the other, unconfined, buckled mode (Fig. 1). This snap-through instability is the same dynamic instability that governs the jumping of popping toys and jumpers by shell snapping (25, 26), but is reminiscent of the (static)

buckling cascade studied previously (27, 28)—hence the name dynamic buckling cascade. A key conceptual advance of our study is that the use of a single linear actuator for a sequence of automatic, sequentially occurring functions, namely energy storage, then latching, triggering, and jumping. This design makes frugal use of parts and enables practical lightweight and high energy density insect-scale robots to match or exceed the performance of both current existing jumping robots and jumping insects. Given the generality of this design and the importance of the unidirectional loading property, we refer to a machine that Jumps with Unidirectional Muscles and Power Amplification as a "JUMPA." We integrate these principles to demonstrate two robotic innovations: the first is the ability to generate and store the required elastic energy onboard and hence jump twice without the need for manual or external energy storage; and the second is an untethered, self-powered robot carrying an onboard battery, a microcontroller, a sensor, and a printed circuit board (PCB) to sense an external signal, generate a command to activate the muscles, and thereby trigger the jump.

The robot's performance relies on the mechanics of dynamic buckling cascading. We conceive four variations of JUMPAs in which the large stroke of coiled artificial muscles under external heating by a heat gun or electrical heating wires drives the dynamic buckling cascade. Coiled artificial muscles have a high energy-to-weight ratio with impeccable qualities when compared to traditional actuators with respect to cost, availability, working mechanism, and application (29–34). A single stroke generates and stores sufficient energy in the buckled state and causes its self-triggered release to power the jump. We characterize the jumping performance of all robots and introduce a simplified nonlinear spring-mass model to explain the mechanism of jumping by snapping without jointed appendages and predict their trajectory. We define two new quantitative measures for high-performance jumping: the escape time (the time taken for the robot to move, from rest, by a body length) and the elastic energy density (the total energy that can be stored by the actuator in the mechanism, normalized by its volume). In this design space, our robots match or exceed the jumps of both existing robots, which typically have a high energy density, and insects, which have a small escape time.

Results

Robot Design Process. We designed and tested four main variations of the dynamic buckling cascade to maximize jumping height while minimizing size and weight and ensuring fracture resistance. Inspired by evolutionary processes observed in nature, we considered four different configurations, that we refer to as phenotypes, depending on the buckling mode shapes and the initial energy prestorage, as shown in Fig. 2 *A* and *B*: i) asymmetrical beam with prestored energy (AsP), ii) symmetrical beam with prestored energy (SyP), iii) asymmetrical beam without prestored energy (As), and iv) symmetrical beam without prestored energy (Sy). The design space leading to each phenotype includes the selection of the artificial muscles, the desired beam shapes, the triggering mechanics, and the geometry of the robot body. We use a continuous digital light manufacturing (CDLM) 3-dimensional printer to directly print the robot body. Spring steel 1095 is chosen as the material for the snapping beam, due to its high Young's modulus and high yield strength. The thickness of the beam is 50 µm, minimizing the yielding effect during buckling and snapping. This combination of precision additive manufacturing and strong compact actuators, namely coiled artificial muscles, enables insect-scale jumping robots. For cases (i, AsP) and (ii, SyP) which have prestored energy, the beams are manually compressed

Fig. 1. Bioinspiration and principle of operation of the jumping robot. (*A*) Click beetles amplify muscle power through morphology to produce extremely fast movements by "clicking" their bodies to generate jumps for hunting and escape, while other insects (e.g., locusts) initiate jumping by the traditional means of jointed appendages. (*B*) Concept of an insect-scale robot capable of slowly storing elastic energy in buckled beams by the contraction of coiled artificial muscles and the quick release of stored energy by triggering beam snap-through to achieve effective jumping without legs.

to the desired shape near their critical snapping point, and the muscles are used to further compress the beam to self-trigger the snap-through. These two configurations can hence jump only once without manual intervention. A tremendous level of small yet critical details in the robot body were evolved through hundreds of iterations, enabled by 3D printing, to ensure the robot's resilience against the action of the muscles and the beam's output forces, and damage when it hits the ground. For each robot, the muscle's force and stroke were tuned along with the amount of precompression—in the case of AsP and SyP—to enable faster snap-through and increase the jumping height. Eventually, each robot demonstrated a maximum jump height distinct from the other configurations even though they all use the same beam. The snap-through and takeoff durations are only about 4 ms, and the jumpers reach their peak height and then land on the ground all-within about 0.5 s.

Fig. 2*A* illustrates the evolution pathways of these designs. Starting from the general concept of triggering the snap-through by compressing the beam longitudinally, we designed the first-generation robot with a rigid rail on which the snapping beam slides, to thereby restrict the beam's transverse motion. This design then evolved through three major pathways, which have different methods to enable the snap-through of the buckled beam, namely end rotation, rail bending, and precompression. The color change in the figure indicates significant modifications in the robot design leading to the next-generation robots. The robots were tuned by adding or modifying design details in each iteration, such as reducing the size of the robot to fit the capability of the muscles, adding a rotational block and a protrusion to push the buckling beam, changing the boundary conditions of the beam to ensure the desired buckling direction, adding a top beam to enable consecutive jumping, etc. The robot designs ultimately landed into four categories depending on the buckling mode shapes and the initial energy prestorage. Detailed explanations of the various designs of Fig. 2*A* are provided in *SI Appendix*. For example, the compressional triggering has the longest evolution pathway, leading to three of the final robot designs (refer to Fig. 2*B*).

This robot design process combines elements of trial-and-error, frequently used by engineers for prototype development, with elements more akin to natural evolution or evolutionary algorithms. For example, while actuators found to be too weak to initiate jumping were replaced with stronger ones at later stages (trial-and-error), the starting seeds were randomly selected and hence had unpredictable performance (of evolution). As shown in Fig. 2, we started with an abstract concept of a robot having three components connected in parallel: a deformable robot body of arbitrary geometry, a coiled artificial muscle actuator, and an elastic energy-storing component. Without a clear understanding of the nonlinear mechanics and multiphysics of buckling, snap-through, and fracture mechanics, the predictability of performance was low. Also, similarly to evolution, no new components were added between iterations. Instead, only properties (e.g., the morphology of the beam, the muscle, and the robot) were tuned based on prior performance, thereby giving the ability to improve this specific trait (trial-and-error).

Snapshots of the typical jump performance of each one of the four configurations are shown in Fig. 3. We observe that with a single beam, the jumping capacity of SyP > AsP > Sy > As. In other words, the robots with prestored energy (stored manually) can always achieve higher jump heights than the ones where artificial muscles are solely used to load the beam. Similarly, symmetric beam buckling modes can transfer higher impulses and lead to higher jumps than asymmetric modes. The detailed analysis of the design and jumping performance is further

discussed in the *Mathematical Modeling* section. Moreover, the Sy robot is capable of consecutive jumping due to an additional beam which provides a larger restoring force (Fig. 3*B*). For the Sy robot, after the first snap-through is triggered, the heat source is removed, and the muscles gradually return to their original length in approximately 200 s. To enable the Sy robot's consecutive jumping, the top beam provides the restoring force to push the artificial muscles and the robot body back to their original length after the external heat source is removed. The snapped (bottom) beam will also return to its original stable state aided by the top beam which reduces the lateral compression on the robot body during cooling. After that, a second beam snap-through can be triggered like the previous one (though to jump, the robot must be righted manually). The complete consecutive jumping process is illustrated in Movie S2. To our knowledge, this is the smallest engineered jumper capable of two consecutive jumps with onboard elastic energy storage.

Furthermore, we designed a miniature robot that carries the sensor, microcontroller, and battery onboard. Since these components are off-the-shelf and not optimized for macroscale applications, their total size is larger than the robot itself, taking 84% of the total robot mass. With these components, the robot is untethered while having a sensor which detects a light signal and
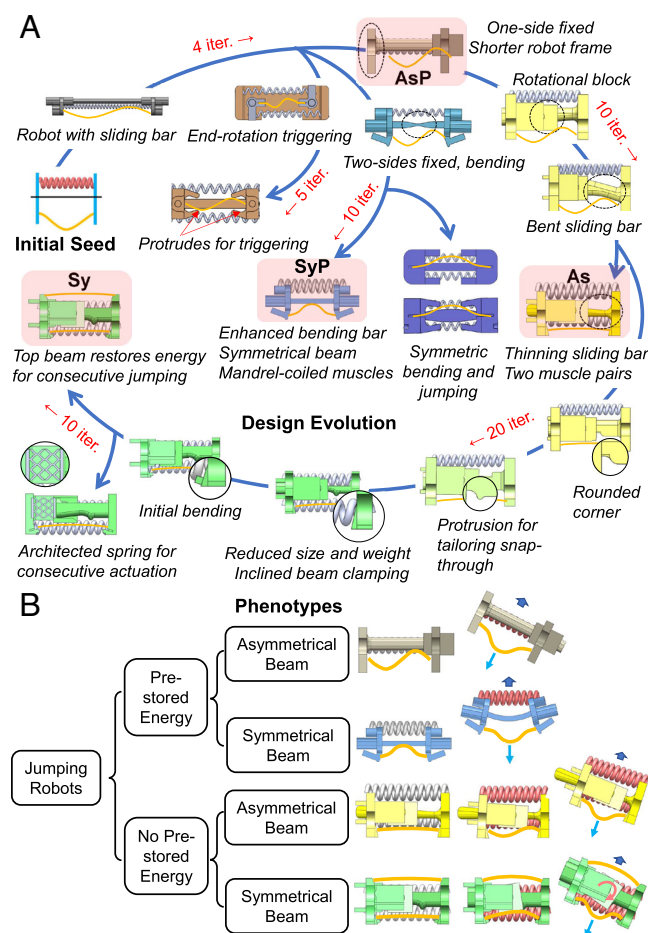
Fig. 2. Evolutionary design cycle and the detailed jumping mechanisms of four robots. (*A*) Design cycle of the jumping robot and evolution of mechanical details as each of the four main phenotypes developed. The coils in these structures are the coiled polymer yarns and the snapping beams are colored orange. *SI Appendix* provides more details for design evolution. (*B*) The buckled beams are categorized into four phenotypes, depending on their buckled shapes and the initial energy status before muscle actuation. AsP, asymmetrical beam with prestored energy; SyP, symmetrical beam with prestored energy; As, asymmetrical beam; Sy: symmetrical beam.
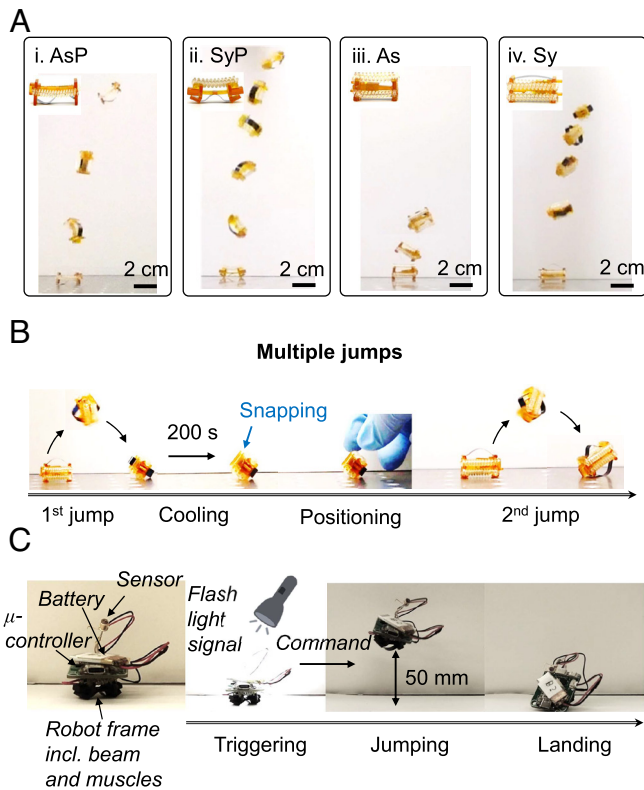
Fig. 3. Jumping performance of the robots. (*A*) Video frames of projectile motion of the jumping robots until reaching the maximum jumping height. (*B*) Mechanism of multiple consecutive jumps of the robot. (*C*) A jumping robot powered by an onboard battery, a microcontroller and a light sensor. When this robot senses a flashlight, a command is issued by the onboard microcontroller to activate the artificial muscles, thereby triggering a jump. The combined mass of the sensor, microcontroller, and battery is 11.4 g so that the total mass of the robot is 13.6 g.

a microcontroller which issues a command to trigger the heating of the muscles for jumping, as illustrated in Fig. 3*C* and Movie S6. The PCB consists of a microcontroller connected to an illumination sensor and a metal-oxide-semiconductor field-effect transistor which can switch on the power to the actuator. Even with these heavy off-the-shelf components, the robot jumps 2.5× times its own body length. While this robot is not "fully autonomous" as detailed in the *Discussion* section, these advancements demonstrate the potential capabilities for system-level autonomous jumping by triggering a control command in response to an external signal and confirm the efficiency of the buckling cascading in JUMPA robots.

**Mechanics of Dynamic Buckling Cascades and Artificial Muscles.** We characterized the mechanics of the dynamic buckling cascade of the beam in each configuration to design the robot and tailor the artificial muscle. We used mechanical testing on an Instron universal testing machine. We designed special holders to apply longitudinal forces on the beam to buckle them and/or trigger their snap-through. Fig. 4*A* and Movie S5 show the self-triggering and beam shape evolution during the dynamic buckling cascade. The robot design for the i) AsP phenotype compresses one end of the beam by sliding against a rigid rail, and the snap-through is automatically self-triggered when the elastic beam becomes unstable when strongly pushed against the rail (Fig. 4*A*). As shown in Fig. 4*B*, an end displacement of only 0.42 mm, along with a force increase of 0.05 N, is needed to trigger the snap-through of AsP, which is the smallest among all four cases. The shape of the elastic beam before and after snap-through is shown in Fig. 4*C*.

The beam is asymmetric right before snap-through but becomes symmetric as it reaches the other stable configuration. We note that the robot is fixed to the testing machine during these tests, and hence, no interaction between the beam and ground is involved.

The JUMPA design for (ii) SyP phenotype replaces the sliding bar with a flexible robot body. Upon compression, the flexible rail bends and causes rotation of the fixed ends of the prebuckled beam. This snap-through mode is hence triggered by the angular rotation of the beam clamps. The force–displacement profiles for this snap-through are in Fig. 4*B*, and the shape-changing of the elastic beam is in Fig. 4*C*. Similar to AsP, this snap-through configuration requires small triggering force and stroke, yet it provides the highest jump height. We attribute this to the fast growth of the symmetric mode and force capacity compared to asymmetric beam configurations.

Dynamic buckling cascade concepts can fully rely on onboard muscles to load the beam and hence achieve multiple jumps. The loading stage requires larger actuation strains and forces from the muscles (see cases As and Sy in Fig. 4*B* for example). As the linear stroke of a single muscle is 15%, the mechanism should store as much energy as possible within this limit and be able to reach the self-triggered snap-through at the end of the energy storage process. Tens of design iterations were performed to tailor the small details on the robot body, specifically the beam clamps and joints. First, for the case of an asymmetrical beam, the sliding rigid rail has an inclined upper surface. A pair of muscles is installed on the upper side of the robot. The beam at the bottom is compressed laterally and rotates at both ends simultaneously, resulting in a snap-through. The Sy robot design consists of two buckling beams on either side of the robot body, a rotator, and a protrusion on the sliding rigid rail (case iv in Fig. 3). The beam on the upper side is used to provide restoring force to push the muscles and the other beam back to their initial states after snap-through for the next actuation cycle, so that the robot can achieve consecutive jumps. To ensure that the beam on the bottom side is buckled upward upon lateral compression, the beam is plastically deformed to a small bending angle of 10° before assembly. At the beginning of each actuation cycle, the beam is free from compression. When the muscles contract, the beam buckles upward and touches the rotator, pushing the rotator anti-clockwise. The beam forms an "M" shape, and when the rotator reaches the protrusion, the rotator starts rotating clockwise due to the curvature of the rotator and the protrusion. This clockwise rotation pushes the beam downward and triggers the snap-through (Fig. 4*A* and Movie S2). Case iv, Sy, which consists of two beams and is capable of consecutive jumps, requires the largest actuation force (13 N) and 1.4 mm linear strain. The beam shapes at different time instances are shown in Fig. 4*C* for all four cases. The curve on the bottom of each figure represents the shape of the beam after snap-through, and other curves show how the beam is gradually compressed until snap-through occurs. The artificial muscles' geometry and performance were tailored to match the mechanical requirements of the snapping beams in insect-scale jumping robots (muscle tailoring details are in *SI Appendix*). For the "Sy" phenotype, which places the most stringent requirements on the muscles since the energy loading of the beam must be performed by one stroke of the muscles, three muscles (M1 to M3) were considered to achieve the required force and stroke of 13 N and 7% (Fig. 4*D* and *SI Appendix*).

Jumping Performance. The high-frame-rate video reveals the critical role of the ground interaction during the robot's takeoff, which lasts only about 4 ms. Fig. 5*A* shows video frames of the buckling beams and the ground for the duration of ground interaction for all four cases (Movies S1, S2, and S4). For robots with asymmetrical beams (i and iii), a portion of the buckled
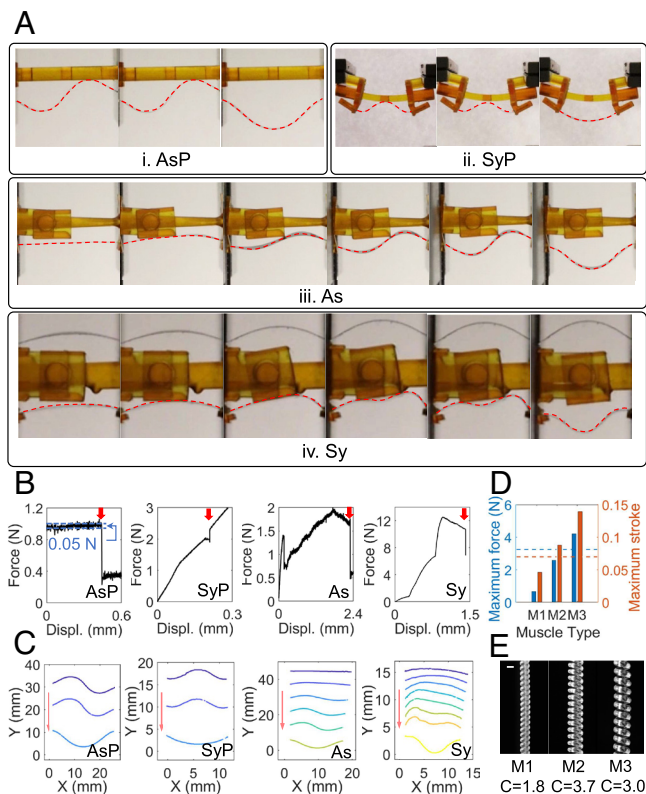
Fig. 4. Triggering and muscle development for snap-through of the bucking beams. (*A*) Video frames during compression for all four phenotypes by an Instron mechanical tester to show left-to-right the evolution of buckling beam shapes during actuation (including compression and snap-through). The dashed blue and orange lines indicate the required force and stroke to actuate the robots. (*B*) Force–displacement curves for the buckling beam during compression and snap-through for all four cases. Red arrows point to the snap-through locations. (*C*) Shape evolution of the buckling beams with increasing time (*Top* to *Bottom*) throughout actuation for the four phenotypes. (*D*) Comparison of three developed coiled muscles, pictured in *E*, against the criteria for jumping, namely maximum force in an isometric test and maximum stroke in an isobaric test under 4 N constant load. (*E*) Images of the tailored artificial muscles with different spring indices, C. The scale bar represents 1mm.

beams is in contact with the ground before snapping. When the snap-through starts, the other half of the beam quickly moves downward and the entire beam interacts with the ground, releasing energy. In contrast, robots with symmetrical beams (ii and iv) do not have any portion of the beams on the ground before snap-through starts. The beams have one or two points hitting the ground and push the robot body to leave the ground with a rapidly increasing takeoff velocity. Fig. 5*B* illustrates the beam shapes at different instants of time when interacting with the ground. (The curve on the top and bottom of each figure represents the shape of the beam at the onset of snap-through and when leaving the ground, respectively.) Generally, robots with prestressed beams exhibit faster ground interaction than those without prestored beams, and robots with symmetrical beams also interact with the ground for a shorter time than those with asymmetrical beams. For example, the robot based on the asymmetrical beam with prestored energy has the shortest ground contact time of 2 ms, and the robot based on the asymmetrical beam without prestored energy has the longest ground contact time of 6 ms.

Next, we describe the essential performance metrics of jumping and benchmark the jumping height of JUMPA robots with various beam configurations against that of insects (1, 3, 4, 9–11, 35–41), and previous robots (15–17, 42–50). In Fig. 5*C*, we plot the raw jumping data, namely jump height versus size (maximum body length). On this logarithmic plot, the line with a slope of 1 shows

insects and robots whose jump is equal to 10 times their size. As can be seen, insects are impressive jumpers as they all exceed this metric. The Sy phenotype robot lies above this line without prestored energy, while the SyP+ robot reaches our record jump height of 890 mm when five beams are used (though it then relies on prestored energy).

Next, we compare the metrics underlying the jumping performance starting with the potential energy, mgH with H the jump height; this is expected to correlate with the stored elastic energy $U = \bar{u}L^3$ where $\bar{u}$ is the mean elastic energy density. Assuming that the elastic energy is efficiently transferred to kinetic energy when the robot jumps, we can write $\bar{u} \sim \dfrac{mgH}{L^3}$, and will use this as the y-axis performance metric. We consider the second most important metric to be the escape time τ of robots and insects, defined as the time taken to move by a body length L. This distance is related to the mean acceleration of the robot by $L = \dfrac{1}{2}\bar{a}\tau^2$. We can express then the escape time τ scaling as $\left(\dfrac{L}{\bar{a}}\right)^{\frac{1}{2}}$. In Fig. 5*D*, we plot $\bar{u} \sim \dfrac{mgH}{L^3}$ versus $\tau \sim \left(\dfrac{L}{\bar{a}}\right)^{\frac{1}{2}}$. Robots achieve higher energy density than insects because most robots, including ours, use spring steel storage elements (helical springs or buckling beams) which have an extremely high strain energy density
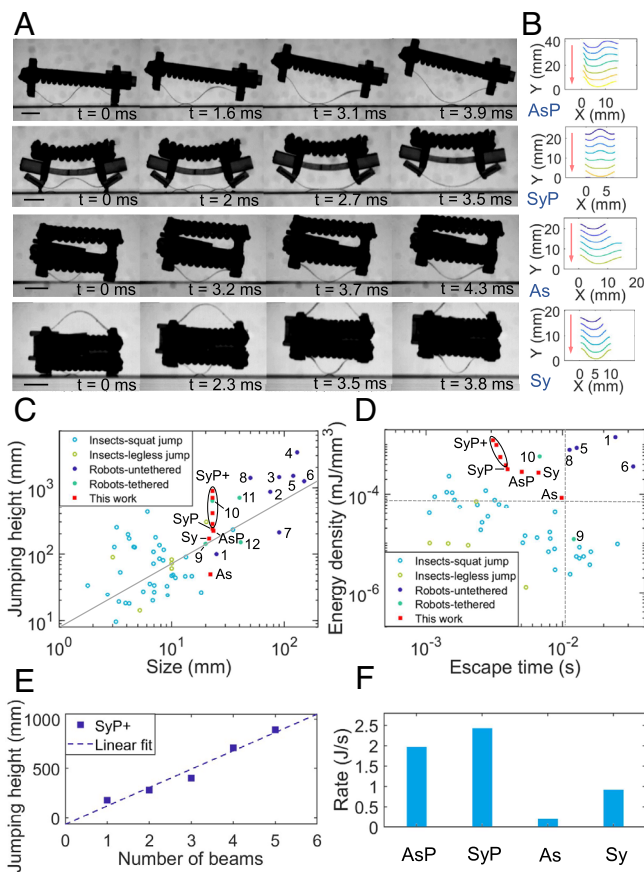
Fig. 5. Close-up slow-motion view of robot jumping mechanism and performance. (*A*) High-speed camera video frames of the beam snap-through and the ground interaction process for all four phenotypes. (*B*) Shape evolution of the buckling beams at different times during actuation of the four phenotypes. (*C*) Comparison of various insects, previous jumping robots, and this work in terms of jumping heights and sizes (maximum body length). (*D*) Comparison of various insects, previous jumping robots, and this work in terms of energy density and escape time. (*E*) Jumping height of the robots using more than one symmetrical buckling beams acting in parallel, with prestored energy (SyP+ phenotype), as a function of the number of these beams. (*F*) Energy release rate during the snap-through of the four phenotypes.

enabled by the high stiffness and strength of steel compared to natural materials. Moreover, our robots not only match the highest elastic energy stored in the literature but also achieve this at a much smaller size. However, the plot also shows that previous robots have a slower escape time than is typical of insects (on this plot, the shorter the time scale, the higher the ability of the robot to escape). We observe that our robots have much shorter escape time than any other man-made robot and, further, that they match the performance of insects, reflecting the extremely high acceleration of these robots achieved at their small size. Overall, Fig. 5D demonstrates that the dynamic buckling cascading is an extremely effective design to actuate and amplify robot jumping at small scales, and it is a promising concept for adoption. A table containing the robot and insect data is provided in *SI Appendix*.

Mathematical Modeling. To investigate the mechanism of a dynamic buckling cascade and make quantitative predictions about the robot's jumping height and velocity, we used the simple lumped mass-spring model illustrated schematically in Fig. 6A. This model, which captures only the snap-through stage, incorporates the essential physics of jumping: the robot has a large mass whose jumping is actuated by the snap-through of an elastic element with a smaller mass. The simplest element able to snap in this way is a bistable von Mises truss: a central mass (m_b) connected to two springs, sandwiched between two immobile boundaries with precompression when the springs are horizontal. The outer boundaries represent the mass of the robot (m_r) while the central mass and springs represent the mass and elasticity of the beam (Fig. 6 A, i). Here, we fix the motion of both the central and edge masses to take place only along the vertical direction. The jump is latched by pushing the central mass to the horizontal position (i.e., $y_b = 0$, see Fig. 6 A, ii), compressing the springs in the process. With a small perturbation, the central mass snaps downward (Fig. 6 A, iii), and the motion is controlled by Newton's second law beyond this point. We find, as expected, that the central mass hits the substrate (see Fig. 6 A, v, so that $y_b = -d$, where d is the height of the beam mass relative to the substrate, as shown in Fig. 6 A, i). Somewhat surprisingly, before this occurs, the edge masses lose contact with the substrate at a specific point (from Fig. 6 A, iii–v). Ultimately, the central mass itself also takes off (Fig. 6 A, vi).

More quantitatively, we write Newton's second law for the motion of each mass in the system (the robot and the central mass) that accounts for the inertia of each mass, the spring forces on each mass, the weight of the robot, and any reaction force from the ground (which is only present during contact). (Note that we neglect the weight of the central mass, since it is much lighter than the outer masses, but retain its inertia since we must be able to track its position.) This gives that the positions of the masses m_b and m_r, denoted y_b and y_r, respectively, satisfy the second-order differential equations:

$$m_b \frac{d^2 y_b}{dt^2} = -2k(y_b - y_r)\left\{1 - \frac{l_0}{\left[w^2 + (y_b - y_r)^2\right]^{\frac{1}{2}}}\right\} + R_b, \quad [1]$$

and

$$m_r \frac{d^2 y_r}{dt^2} = k(y_b - y_r)\left\{1 - \frac{l_0}{\left[w^2 + (y_b - y_r)^2\right]^{\frac{1}{2}}}\right\} - m_r g + R_r. \quad [2]$$

Here, R_b and R_r represent the ground reaction forces on each mass, which are required to ensure no penetration into the ground and are only nonzero when the relevant mass is in contact with the ground (i.e., $R_r \geq 0$ when $y_r = 0$ and $R_b \geq 0$ when $y_b = -d$). By solving these equations subject to the constraints $R_{b,r} \geq 0$, $y_r \geq 0$, $y_b \geq -d$, we find that the process of jumping evolves through four distinct phases, which are illustrated schematically in panels of Fig. 6 A, iii–vi. The properties of each phase are studied in detail in *SI Appendix*, but in summary the important points in each phase are the following:

1. *Snap-down*: The motion begins with $y_b = -\varepsilon$, $y_r = 0$ and $R_b = 0$; the central mass accelerates toward the substrate, pushed by the force of the relaxing spring. In this phase, the robot masses remain at their initial position, $y_r = 0$, and the reaction force R_r decreases, remaining in the interval $0 < R_r < m_r g$.

2. *Ghost jump*: As the central mass accelerates downward, but before it contacts the substrate, the reaction force of the substrate on the edges vanishes: $R_r = 0$. As a result of the downward acceleration of the central mass, the outer masses are slightly lifted from the ground; in general, this is a slow acceleration, and neglecting it aids our analytical work with minimal loss of accuracy in the predictions of the model.

3. *Driven jump*: Once the central mass contacts the substrate, $y_b = -d$ and $R_b > 0$; and m_r begins a more concerted jump in which the full force of the spring acts to drive the robot upward.

4. *Total loss of contact*: The whole robot (both m_r and m_b) takes off from the ground when the compression within the spring is fully released. The robot then follows the usual projectile motion, albeit coupled with a weak oscillation induced by the tension and compression of the spring.

By applying appropriate initial conditions, the equations of motion [1] and [2] can be solved through each of these different stages in turn to quantitatively predict the jumping motion. More specifically, at each stage, the differential equations of motion are solved numerically by employing the routine ode15s in Matlab. All the (physical and geometric) parameters are measured from experiments (as given in *SI Appendix*, Table S1), except for the spring stiffness, k. Since we are considering four designs of robot in experiments with different physical and geometric parameters, we treated the exact value of the spring stiffness as a single fitting parameter for each of the four robots (Fig. 6 B and C). The fitting to obtain k is performed once for the SyP robot even as the restriction height changes. As a comparison, the expected order of magnitude of k can be found by equating the stored energy in the latched state of the model system with that in the beam elements of the real robot; this yields an estimate that is within approximately 50% of the fitted value.

To evaluate the model, we performed systematic experiments where we use the same robot with different jumping conditions. We used recorded videos from experiments to analyze the displacement and velocity of jumping under four different boundary and energy storage conditions. Fig. 6C shows the velocity of each robot body throughout the duration of the beam's interaction with the ground. Robots with faster ground interaction generate higher take-off velocity measured at the instant when the snapping beam leaves the ground and vice versa (Fig. 6C). Typical predictions of the model for the evolution of the robot's vertical displacement and upward velocity are shown in Fig. 6 B and C, respectively, and are compared with experimental measurements. A good agreement between theory and experiment is found for both the displacement and velocity evolution for all four cases. However, we note that the model breaks down somewhat toward the end of each jump: the predicted velocity gradually levels off, while the experimentally observed velocity does not. We attribute this

deviation to the breakdown of our spring model as contact is lost: our simple spring model does not account for the rapid decrease in the contact area for a beam at the end of contact and so the point of zero acceleration (plateau velocity) happens more suddenly experimentally than predicted in the model.

We observed that the jumping height can be tuned by the timing of the beam impulse. To investigate this important effect, we evaluated jumping robots with different restriction heights (h_R), defined as the distance between the lower stable position of the buckling beam and the ground (as shown in the *Inset* of Fig. 6D). This definition shows that a larger h_R would cause the ground to "interfere" earlier with the snapping beam during its downward snapthrough. We plot the accelerations of the robot (predicted by the von Mises truss model) with a symmetrical beam and prestored energy (SyP) for four different restriction heights (Fig. 6D). We observe that h_R causes an abrupt transition from phase 2 (Ghost jump) to phase 3 (Driven jump). We note that the rate of change of acceleration (the "jerk") in phase 2 is extremely high, and the maximum acceleration is reached when the beams reach the maximum amplitude in the other stable configuration. Hence, minimal changes in the restriction height, on the order of millimeters, can change the acceleration at the onset of phase 3. Since the restriction height should not exceed the height of the midpoint of the buckled beam, $h_0 = \sqrt{l_0^2 - w^2}$, see Fig. 6 D, *Inset*, we therefore plot the takeoff velocity as a function of $h_R = h_0 - d$ in a wide range ($0 < h_R < h_0$) for both experiments (blue dot) and numerical calculations (yellow line), as shown in Fig. 6E. This clearly shows that the takeoff velocity increases with increasing restriction height, consistent with the increase of the acceleration duration as shown in Fig. 6D. However, the takeoff velocity ultimately saturates with a plateau when h_R approaches some upper limit. We also observe that the duration of positive acceleration increases with increasing h_R. As a result, the takeoff velocities of the robot also monotonically increase with h_R, as shown in Fig. 6E. These results suggest that the jumping abilities of robots can be optimized by modifying their geometric parameters. A small protrusion at the beam clamping point of no more than 2 mm can increase the jump height twofold!

To further understand the effect of the restriction height on the final jumping velocity and guide the optimization of the jumping robot, we return to the bistable truss model and obtain an approximate analytical solution by neglecting the ghost jump phase (see *SI Appendix* for details). This calculation shows that the jump velocity is given approximately by

$$v_{jump}^2 = \frac{2k}{m_r} \cdot \left\{ l_0 \left[l_0 - \sqrt{w^2 + \left(\sqrt{l_0^2 - w^2} - h_R \right)^2} \right] \right.$$
$$\left. - \frac{1}{2} \left[l_0^2 - w^2 - \left(\sqrt{l_0^2 - w^2} - h_R \right)^2 \right] - 2\mu_0 h_R \right\}. \quad [3]$$

We plot the analytical prediction for the takeoff velocity, Eq. **3**, in Fig. 6E (see the magenta curve) and find that, over much of the range of h_R, this approximate analytical solution matches the numerical calculations very well. From the plot of the analytical solution, we note the linear dependence of the takeoff velocity on h_R for small values of h_R. This relationship results from the small residual elastic energy remaining in the spring at the moment of contact (which may be shown to be proportional to h_R^2, see *SI Appendix*)—this residual energy is converted to the kinetic energy of the robot after contact giving
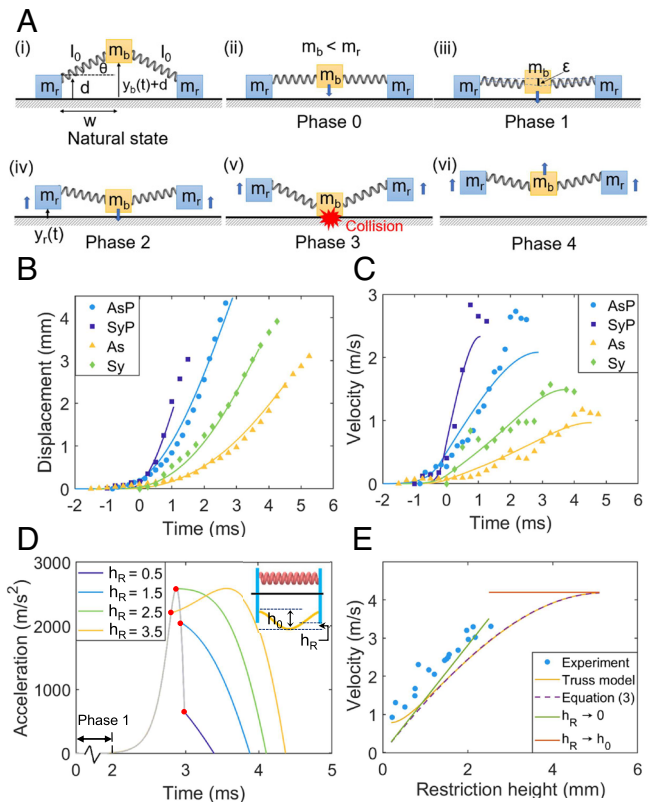
Fig. 6. Reduced-order model of the robot jumping mechanism using a von Mises truss. (A) Schematic of the von Mises truss model used to analyze the robot jumping mechanism. The blue arrows show the direction of motion. The four phases of motion are listed in the main text. (B) Experimental results (markers) and theoretical predictions (solid lines) of the vertical displacement as a function of time during buckling beam–ground interaction. (Here, we shift the data horizontally to match the starting point of interaction.) (C) Vertical velocity as a function of time for the robot body during buckling beam-ground interaction. The solid curves in B and C represent the simulation results from the von Mises truss model. (D) Vertical acceleration of the robot as a function of time during jumping for different restriction heights (h_R, as schematically marked in the *Inset*). The gray solid curve indicates the acceleration during phase 2, after which lines with different colors represent the acceleration during phase 3 with different restriction heights. The transition points between phase 2 and phase 3 are marked with red circles. (E) The takeoff velocity as a function of restriction height is illustrated by experimental data points and theoretical predictions (both the numerical calculation and the simplified explicit formula). Green line represents takeoff velocity on h_R for small values of h_R (refer to Eq. **4** in the main text), and the orange line represents the case of large restriction height, i.e., $h_R \rightarrow h_0$ (refer to Eq. **5** in the main text).

$$v_{jump} \approx \sqrt{\frac{k}{m_r}} \frac{h_0}{l_0} \cdot h_R, \quad [4]$$

see the green line in Fig. 6E. (Crucially, however, the initial kinetic energy of the beam is dissipated in impact.) Conversely, in the case of large restriction height, i.e., $h_R \rightarrow h_0$, we find that all of the elastic energy initially stored in the buckled beam transfers to the robot as kinetic energy (*SI Appendix*), so that

$$v_{jump} \approx \sqrt{\frac{k}{m_r}} (l_0 - w); \quad [5]$$

this is the plateau illustrated by the orange line in Fig. 6E. (In this case, very little energy is dissipated in impact because the beam mass is not traveling fast at the moment of impact.)

Discussion

In this work, we described the design of insect-scale jumping robots and their jumping capabilities, showing that by using a dynamic buckling cascade these robots can combine the best performance attributes of both robots and insects. The dynamic buckling cascade is realized by snapping beams actuated by coiled artificial muscles and achieves a low part count, high forces, and high accelerations via a sequence of self-evolving buckling modes thereby covering all the necessary steps for jumping from energy storage to triggering and release. Our design benefits from the high force and stroke of coiled muscles, and the fast snap-through of a buckling beam to achieve high-power amplification. Overall, the results improve our understanding of impulsive momentum exchange mechanisms, and more specifically the ground interactions that lead to jumping.

We investigated four main variations, referred to as phenotypes, of the dynamic buckling cascade, including the effect of different buckling mode configurations. Among all four phenotypes investigated, the robot based on the symmetrical beam with prestored energy had the highest energy release rate and thus highest jumping. In addition, robots based on beams without prestored energy can perform consecutive jumps by actuation-restoring cycles, but at the cost of lower jumping height compared to preloaded cases. Since only triggering is required for preloaded cases, large elastic energy can be stored in the buckled beams manually, which can still be triggered by the muscles. Our experiments and theory highlight the critical role of ground interaction through a parameter we call the restriction height, which sensitively controls the takeoff velocity of the robot.

We developed the robot designs through iterative trial and error enabled by high-precision additive manufacturing. We note that for a simple jumping robot based on a dynamic buckling cascade, there is currently no mathematical design optimization algorithm capable of finding a globally optimal jumper due to the complex multiphysics of this problem (nonlinear mechanics, dynamics, manufacturability, material selection). In retrospect, this iterative design approach is reminiscent of evolution by natural selection, where the complexity of the functions and the vastness of the design space precludes existing mathematical design optimizations from finding a global optimal topology. However, we envision that in the future, machine-learning approaches may be trained on evolutionary pathways benchmarked from biological studies for use in the design of robotic functions. Several technical challenges remain, ranging from adding a simple mechanism for controlling, up to readjusting the landing orientation.

The miniature robot developed here has most of the hardware required to be fully autonomous: it has sensors, controller, and batteries onboard, but cannot self-right (in case it lands upside down) and steer. Inspired by the definitions of "full self-driving" issued by the Society of Automotive Engineers SAE J3016, we propose (*SI Appendix*, Table S6) criteria for six levels of autonomy for insect-scale robots. According to these criteria, the nonsteerable robots presented here are not yet fully autonomous, because the robot does not have self-righting or steering abilities.

The framework in this study will enable other impulsive mechanisms such as piercing, hammering, fast deployment, needle insertion, and burrowing. Some of these applications can be further miniaturized to extremely small scales by using the low part count afforded by the dynamic buckling cascade. We anticipate that in the future fleets of insect-inspired robots can be adapted for use in natural disaster scenarios, search and rescue missions, hazardous environments, or other critical relief situations where larger robotic platforms are inaccessible, and jumping is the most effective mobility at small scale.

Materials and Methods

Robot Materials and Fabrication. The robot body was fabricated by a CDLM 3D printer (Micro Plus cDLM, EnvisionTEC). E-Partial was obtained from EnvisionTEC and printed with a 25-micron resolution to fabricate the robot body. The robot body for (ii) a symmetrical beam with prestored energy was directly used after printing, while others were ultraviolet cured at 60 °C for 90 min to obtain more rigid structures and smoother surfaces. Buckling beams were fabricated from spring steel 1095 purchased from McMaster-Carr. The beam thickness was 50.8 μm, and other dimensions for each robot are detailed in *SI Appendix*, Table S1.

The coiled artificial muscles were fabricated using nylon 6 fibers with a diameter of 1 mm that were purchased from AGOOL. The precursor fiber was first tied on one end to a motor and the other end to a linearly guided deadweight of 800 g. The end of the deadweight was also fixed perpendicular to the rotational axis to restrict rotation around the rotational axis. The motor rotates and twists the fiber until the thread is completely coiled on a water-solvable mandrel. The fabrication process was followed by annealing in oil at 120 °C for 3 h. The coiled artificial muscle with mandrel was then immersed in water at 45 °C for 3 d to dissolve the mandrel. Next, the artificial muscle underwent the second annealing in oil at 180° for 8 h to maintain the coiled shape. The fabricated muscle had an outer diameter of 3.5 mm and pitches of 0.8 mm. The measured stiffness of the artificial muscles was 2,100 N/m.

Experimental Setup and Procedures. Robot takeoff and landing experiments were conducted on a stainless-steel surface, and the artificial muscles were actuated using a heat gun from a 50 cm distance. We filmed the robot takeoff and landing using a Sony Cyber-shot DSC-RX100 VII Digital Camera at a frame rate of 60 fps. The high-speed videos were recorded by a Fastec HiSpec 5 camera at a frame rate of 6,000 fps. We tracked the locomotion of the robots and snapping beams using ProAnalyst motion analysis software.

The actuation force versus displacement relationship of the buckling beam during compression and snap-through was measured on a tensile test machine (Instron ElectroPuls E1000). The images and videos were recorded by a Canon 60D DSLR camera.

Data, Materials, and Software Availability. All study data are included in the article and/or *SI Appendix*.

Author affiliations: ªDepartment of Mechanical Science and Engineering, University of Illinois at Urbana-Champaign, Urbana, IL 61801; ᵇMathematical Institute, University of Oxford, Oxford OX2 6GG, United Kingdom; ᶜDepartment of Entomology, University of Illinois at Urbana-Champaign, Urbana, IL 61801; ᵈThe Department of Mechanical and Aerospace Engineering, Princeton University, Princeton, NJ 08544; and ᵉAlan G. MacDiarmid NanoTech Institute, University of Texas at Dallas, Richardson, TX 75080

1. S. N. Patek, J. E. Baio, B. L. Fisher, A. V. Suarez, Multifunctionality and mechanical origins: Ballistic jaw propulsion in trap-jaw ants. *Proc. Natl. Acad. Sci. U.S.A.* **103**, 12787–12792 (2006).
2. O. Bolmin *et al.*, Latching of the click beetle (Coleoptera: Elateridae) thoracic hinge enabled by the morphology and mechanics of conformal structures. *J. Exp. Biol.* **222**, jeb196683 (2019).
3. M. Burrows, Jumping performance of froghopper insects. *J. Exp. Biol.* **209**, 4607–4621 (2006).
4. M. Burrows, Jumping mechanisms and performance of snow fleas (Mecoptera, Boreidae). *J. Exp. Biol.* **214**, 2362–2374 (2011).
5. M. Burrows, V. Hartung, H. Hoch, Jumping behaviour in a Gondwanan relict insect (Hemiptera: Coleorryncha: Peloridiidae). *J. Exp. Biol.* **210**, 3311–3318 (2007).
6. J. F. Campbell, H. K. Kaya, How and why a parasitic nematode jumps. *Nature* **397**, 485–486 (1999).

7. R. M. N. Alexander, *Elastic Mechanisms in Animal Movement* (Cambridge University Press, ed. 1, 1988).
8. O. Bolmin *et al.*, Nonlinear elasticity and damping govern ultrafast dynamics in click beetles. *Proc. Natl. Acad. Sci. U.S.A.* **118**, e2014569118 (2021).
9. G. P. Sutton, M. Burrows, Biomechanics of jumping in the flea. *J. Exp. Biol.* **214**, 836–847 (2011).
10. M. Burrows, G. P. Sutton, The effect of leg length on jumping performance of short- and long-legged leafhopper insects. *J. Exp. Biol.* **211**, 1317–1325 (2008).
11. Q. V. Nguyen, H. C. Park, Design and demonstration of a locust-like jumping mechanism for small-scale robots. *J. Bionic Eng.* **9**, 271–281 (2012).
12. V. M. Ortega-Jimenez *et al.*, Directional takeoff, aerial righting, and adhesion landing of semiaquatic springtails. *Proc. Natl. Acad. Sci. U.S.A.* **119**, e2211283119 (2022).
13. G. Ribak, S. Reingold, D. Weihs, The effect of natural substrates on jump height in click-beetles. *Funct. Ecol.* **26**, 493–499 (2012).
14. G. Ribak, O. Mordechay, D. Weihs, Why are there no long distance jumpers among click-beetles (Elateridae)? *Bioinspir. Biomim.* **8**, 036004 (2013).
15. D. W. Haldane, J. K. Yim, R. S. Fearing, "Repetitive extreme-acceleration (14-g) in spatial jumping with Salto-1P" in *IEEE International Conference on Intelligent Robots and Systems* (Institute of Electrical and Electronics Engineers Inc., 2017), pp. 3345–3351.
16. J. Zhao, W. Yan, N. Xi, M. W. Mutka, L. Xiao, "A miniature 25 grams running and jumping robot" in *Proceedings–IEEE International Conference on Robotics and Automation* (Institute of Electrical and Electronics Engineers Inc., 2014), pp. 5115–5120.
17. F. Li *et al.*, Jumping like an insect: Design and dynamic optimization of a jumping mini robot based on bio-mimetic inspiration. *Mechatronics* **22**, 167–176 (2012).
18. W. A. Churaman, A. P. Gerratt, S. Bergbreiter, First leaps toward jumping microrobots. *IEEE Int. Conf. Intell. Robot. Syst.* **2**, 1680–1686 (2011).
19. T. Li *et al.*, Agile and resilient insect-scale robot. *Soft Robot.* **6**, 133–141 (2019).
20. Y. Wu *et al.*, Insect-scale fast moving and ultrarobust soft robot. *Sci. Robot.* **4**, 31 (2019).
21. P. Chirarattananon, K. Y. Ma, R. J. Wood, Perching with a robotic insect using adaptive tracking control and iterative learning control. *Int. J. Rob. Res.* **35**, 1185–1206 (2016).
22. E. W. Hawkes *et al.*, Engineered jumpers overcome biological limits via work multiplication. *Nature* **604**, 657–661 (2022).
23. Z. Zhang, J. Zhao, H. Chen, D. Chen, A survey of bioinspired jumping robot: Takeoff, air posture adjustment, and landing buffer. *Appl. Bionics Biomech.* **2017**, 4780160 (2017).
24. A. Witze, High-jumping beetle inspires agile robots. Published on 13 November 2017, *Nature* (2017).
25. A. Pandey, D. E. Moulton, D. Vella, D. P. Holmes, Dynamics of snapping beams and jumping poppers. *Europhys. Lett.* **105**, 24001 (2014).
26. B. Gorissen, D. Melancon, N. Vasios, M. Torbati, K. Bertoldi, Supplementary materials for inflatable soft jumper inspired by shell snapping. *Sci. Robot.* **5**, 1967 (2020).
27. B. Roman, A. Pocheau, Buckling cascade of thin plates: Forms, constraints and similarity. *Europhys. Lett.* **46**, 602–608 (1999).
28. J. Beharic, T. M. Lucas, C. K. Harnett, Analysis of a compressed bistable buckled beam on a flexible support. *J. Appl. Mech. Trans. ASME* **81**, 081011 (2014).
29. J. Mu *et al.*, Sheath-run artificial muscles. *Science* **365**, 150–155 (2019).
30. C. Lamuta, S. Messelot, S. Tawfick, Theory of the tensile actuation of fiber reinforced coiled muscles. *Smart Mater. Struct.* **27**, 055018 (2018).
31. M. Kanik *et al.*, Strain-programmable fiber-based artificial muscle. *Science* **365**, 145–150 (2019).
32. S. Tawfick, Y. Tang, Stronger artificial muscles, with a twist. *Science* **365**, 125–126 (2019).
33. C. S. Haines *et al.*, New twist on artificial muscles. *Proc. Natl. Acad. Sci. U.S.A.* **113**, 11709–11716 (2016).
34. C. S. Haines *et al.*, Artificial muscles from fishing line and sewing thread. *Science* **343**, 868–872 (2014).
35. M.-C. Cadiergues, C. Joubert, M. Franc, A comparison of jump performances of the dog flea, Ctenocephalides canis (Curtis, 1826) and the cat flea, Ctenocephalides felis felis (Bouché, 1835). *Vet. Parasitol.* **92**, 239–241 (2000).
36. G. Ribak, D. Weihs, Jumping without using legs: The jump of the click-beetles (Elateridae) is morphologically constrained. *PLoS One* **6**, 1–7 (2011).
37. M. A. Bertone, J. C. Gibson, A. E. Seago, T. Yoshida, A. A. Smith, A novel power-amplified jumping behavior in larval beetles (Coleoptera: Laemophloeidae). *PLoS One* **17**, 1–26 (2022).
38. M. Burrows, Jumping mechanisms of treehopper insects (Hemiptera, Auchenorrhyncha, Membracidae). *J. Exp. Biol.* **216**, 788–799 (2013).
39. M. Burrows, Jumping and take-off in a winged scorpion fly (Mecoptera, Panorpa communis). *J. Exp. Biol.* **222**, jeb205385 (2019).
40. M. Burrows, M. Dorosenko, Jumping mechanisms and strategies in moths (Lepidoptera). *J. Exp. Biol.* **218**, 1655–1666 (2015).
41. M. Burrows, M. Dorosenko, Jumping performance of flea hoppers and other mirid bugs (Hemiptera, Miridae). *J. Exp. Biol.* **220**, 1606–1617 (2017).
42. A. Yamada, H. Mameda, H. Mochiyama, H. Fujimoto, "A compact jumping robot utilizing snap-through buckling with bend and twist" in *IEEE/RSJ 2010 International Conference on Intelligent Robots and Systems* (2010), Institute of Electrical and Electronics Engineers (IEEE), Taipei, pp. 389–394.
43. J. Zhao, N. Xi, B. Gao, M. W. Mutka, L. Xiao, "Design and testing of a controllable miniature jumping robot" in *IEEE/RSJ 2010 International Conference on Intelligent Robots and Systems* (2010), Institute of Electrical and Electronics Engineers (IEEE), Taipei, pp. 3346–3351.
44. M. Kovač, M. Fuchs, A. Guignard, J. C. Zufferey, D. Floreano, "A miniature 7g jumping robot" in *Proceedings–IEEE International Conference on Robotics and Automation* (2008), Institute of Electrical and Electronics Engineers (IEEE), Pasadena, pp. 373–378.
45. J. Zhao *et al.*, Controlling aerial maneuver of a miniature-tailed jumping robot. *IEEE/ASME Trans. Mechatron.* **20**, 2903–2914 (2015).
46. V. Zaitsev *et al.*, A locust-inspired miniature jumping robot. *Bioinspir. Biomim.* **10**, 066012 (2015).
47. G. P. Jung *et al.*, JumpRoACH: A trajectory-adjustable integrated jumping-crawling robot. *IEEE/ASME Trans. Mechatron.* **24**, 947–958 (2019).
48. M. Noh, S. W. Kim, S. An, J. S. Koh, K. J. Cho, Flea-inspired catapult mechanism for miniature jumping robots. *IEEE Trans. Robot.* **28**, 1007–1018 (2012).
49. J.-S. Koh *et al.*, Jumping on water: Surface tension-dominated jumping of water striders and robotic insects. *Science* **349**, 517–521 (2015).
50. R. Chen *et al.*, Legless soft robots capable of rapid, continuous, and steered jumping. *Nat. Commun.* **12**, 7028 (2021).